Robotica (2025), **43**, pp. 3888–3901
doi:10.1017/S0263574725102191

CAMBRIDGE UNIVERSITY PRESS

RESEARCH ARTICLE

A comparison of monolithic 3D-printed tendon-driven continuum robot designs

Clara G. Kierbel†, Nicola Perugini† and Matteo Russo

LARM2: Robotics and Mechatronics Laboratory, Department of Industrial Engineering, University of Rome Tor Vergata, Rome, 00133, Italy
Corresponding author: Matteo Russo; Email: matteo.russo@uniroma2.it

Received: 5 March 2025; **Revised:** 16 May 2025; **Accepted:** 28 July 2025; **First published online:** 26 August 2025

Keywords: continuum robots; tendon-driven robots; design; 3D printing

Abstract

This paper presents four new monolithic continuum robot designs that can be 3D printed in a single piece and with TPU or similar elastic filaments for either educational or experimental applications. Similar tendon-driven continuum robots are usually made of a flexible backbone (often in NiTi alloys) and rigid vertebrae, with tens of components in a robot segment resulting in time-consuming manual assembly and high costs. Conversely, the proposed designs achieve equivalent functionality while avoiding the manufacturing challenges. Additionally, by removing the need for coupled features for assembly and 3D-printing backbones and vertebrae as a single part, new geometries are possible and can be explored to tailor robot performance to specific requirements. To validate the proposed design, four sample prototypes have been manufactured and experimentally tested. The obtained results, when compared to the piecewise constant curvature model, demonstrate a 3.06% tip positioning error and limited reduction of the workspace area of 23.07%, which compares favorably to similar but more expensive and complex tendon-driven robots.

1. Introduction

In the past few years, growing interest has been shown in continuum robotics. Compared to conventional rigid-link robots, continuum robots can adapt to their surroundings thanks to their "infinite" number of degrees of freedom (DOFs), making them a great asset in surgery [1, 2], search and rescue [3, 4], various industries such as aeronautics [5, 6] and agriculture [7], and soft grippers [8, 9]. Various categories of continuum robots exist [10]. Among them, the most well-known are the following ones: concentric tube robots [11, 12], which consist of multiple pre-curved tubes that can retract into a main tube; tendon-driven robots, which actuate the devices through cables attached at different levels of the manipulator on one end and to actuators at the other extremities [13, 14]; and fluidic continuum robots [15, 16], which employ antagonistic inflatable chambers or pneumatic muscles to change shape. Tendon-driven manipulators can be designed in many ways, from discrete joint robots [17] to helical spring manipulators [18], among others. Further, new types of continuum robots continue to emerge, such as vine-inspired eversive robots [19, 20].

To create a continuum device, the user needs to consider the choice of actuation, as well as the complexity of modeling, the ease of assembly, and the cost. It is not uncommon for pneumatic continuum robots to be monolithic (e.g., pneunets), but their manufacturing remains complex [21, 22]. Conversely, rod-driven and tendon-driven continuum robots (TDCR) are commonly composed of numerous elements, which can require long and meticulous hours of work to assemble (e.g., the robot in [23] has hundreds of miniaturized components that require a careful manual assembly). Additionally, the manufacturing process of multiple elements can increase the cost of the robot, particularly when

† These authors contributed equally.

© The Author(s), 2025. Published by Cambridge University Press.

https://doi.org/10.1017/S0263574725102191 Published online by Cambridge University Press

high-precision machining is required. The high cost and complex assembly of these robots significantly limit their accessibility, affecting their transfer to industry and the possibility of deploying these robots in specific environments (i.e., radioactive environments would require disposable systems). Furthermore, these factors lead to customized robots being developed for specific tasks [24], further limiting the standardization and benchmark development for this class of robots.

This lack of open-source models, software, and resources is actively hindering the development of continuum robots, which are often developed at a research laboratory up to the Technological Readiness Level 6 and then miss going further, hindered by the lack of resources and regulations [10]. To encourage the development and adoption of continuum robots up to commercial readiness, the accessibility of continuum robotic research must improve, especially from a design perspective. One option to democratize continuum robot design is to focus on the general optimization of the designs of continuum manipulators [25] to improve their efficiency progressively [26]. Another option is the creation and sharing of open-source designs. To this end, some research groups shared their models and data for specific applications: the minimally invasive surgery tendon-actuated device, ENDO, in ref. [27] and the continuum tendon-driven manipulator for underwater remotely operated vehicles in ref. [28]. More general open-source design projects exist for fluidic continuum robots, notably the Soft Robotics Toolkit, created as an educational tool that presents both design, sensing, and control aspects [29, 30]. However, to the best of the authors' knowledge, the only toolkit to specifically address TDCR is the Open Continuum Robotics Project of the Continuum Robotics Laboratory at the University of Toronto [31], which currently provides visualization and simulation tools as well as a generalized actuation module for concentric tube and TDCR, together with an interface to control the actuation module [32]. Other open-source software tools for continuum robots exist, such as SoMo [33].

However, all these open-access tools focus on software and modeling; TDCR designs are usually reported with essential kinematic parameters only, without fully describing the design features or their assembly process, making continuum robot designs hardly reproducible and increasing the barrier to access this research field. For this reason, this paper presents and compares four different continuum robot designs that can be manufactured with easily available materials and technologies. The 3D models of the proposed designs are also included as Supplementary Materials with this paper, providing readers not only with essential kinematic parameters but also with a full knowledge of the entire geometry of the system. This paper expands our previous conference paper [34], which analyzes a single monolithic TDCR, with four new designs. These prototypes all allow for an easy assembly, only requiring the threading of the tendons through their routing channel. Additionally, they can all be printed with off-the-shelf TPU and hobby-grade FDM 3D printers, making the manufacturing affordable and accessible. We then tested the manufactured prototypes to characterize their behavior in terms of reachable workspace and precision with the same actuation unit and evaluation criteria as done in ref. [34]. The experimental results have been compared to identify the strengths and weaknesses of the proposed designs.

2. Robot design

The four robots presented in this article have been designed with the main goal of having a single print to highly simplify the manufacturing process and the assembly, as it allows us to simply add the tendons through their structure. The four designs are modular, made of a specific backbone unit that is then duplicated along the backbone up to the desired backbone length. For ease of comparison, this paper refers to prototypes with shared length (80.00 mm), external diameter (17.50 mm), and internal diameter (3.50 mm), set to match the design previously presented in ref. [34]. However, these dimensions are purely representative, and the system can be scaled according to the capabilities and workspace of the available 3D printers, as well as printing-induced vibrations (which depend on printing speed and on the pressure exerted by the nozzle on the robot backbone while printing), the choice of material and further printing parameters such as infill percentage and pattern, printing temperature, plate temperature, and rafts/brims. Generally, designs from 4 mm up to 200 mm in external diameter can be found in literature,

https://doi.org/10.1017/S0263574725102191 Published online by Cambridge University Press

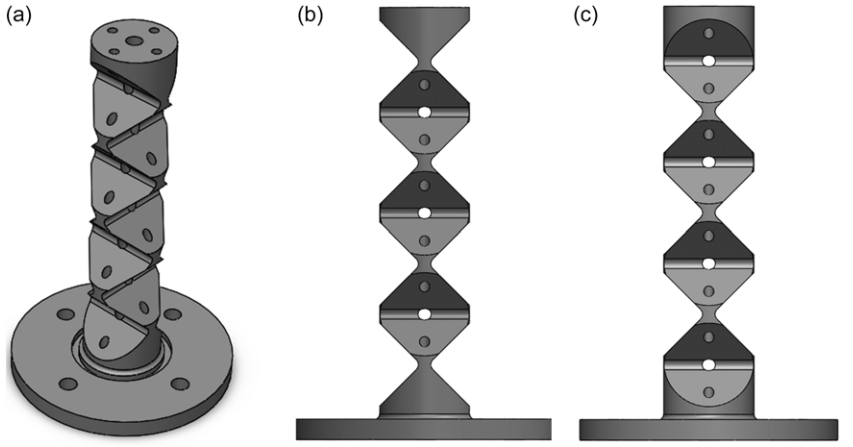


Figure 1. *CAD model of the V-notch design: (a) isometric view; (b) front view; (c) side view.*

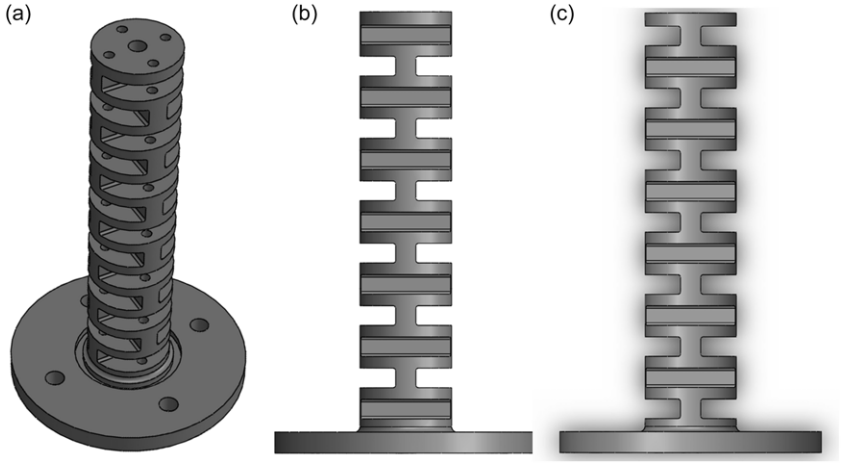


Figure 2. *CAD model of the T-notch design: (a) isometric view; (b) front view; (c) side view.*

with the minimum size being limited by the minimum wall thickness that the 3D printer can manufacture and the maximum size bound by the 3D printer's workspace.

The four designs have been obtained by using common geometries for compliant hinges, allowing for robot bending in one or two directions by reducing local stiffness; at the same time, regions with higher stiffness have been preserved to replicate the tendon-routing functionality of continuum robot vertebrae/disks. The four designs presented all achieve local stiffness variation by reducing cross-section area, according to profiles that allow for smoother or harsher changes: a sawtooth profile (V-notch, linear, Fig. 1), a square wave profile (T-notch, high/low, Fig. 2), a circle arc profile (hourglass, sine, Fig. 3), and a helical profile (helix, Fig. 4).

The first design, presented in Fig. 1, is a circular design with a V-shaped notch pattern on the sides. Consequent notches are designed to allow bending on two perpendicular planes, in order to obtain 3D motion. Fillets have been added at the inner extremity of each notch, allowing for more space for the tendon channels. The notches are set at a 45° angle to allow printing without additional support. Similarly to the other designs, the backbone length (80.00 mm) includes cylindrical segments (height of 2.00 mm each) at each extremity of the main body. An additional base (height of 4.00 mm) is used to attach the design to the actuation system, as well as adding stability and guaranteeing base plate adhesion during the print.

https://doi.org/10.1017/S0263574725102191 Published online by Cambridge University Press

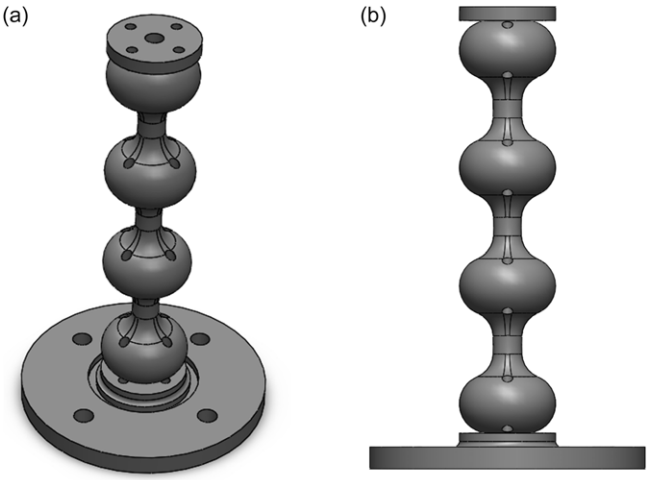


Figure 3. *CAD model of the hourglass design: (a) isometric view; (b) front view.*

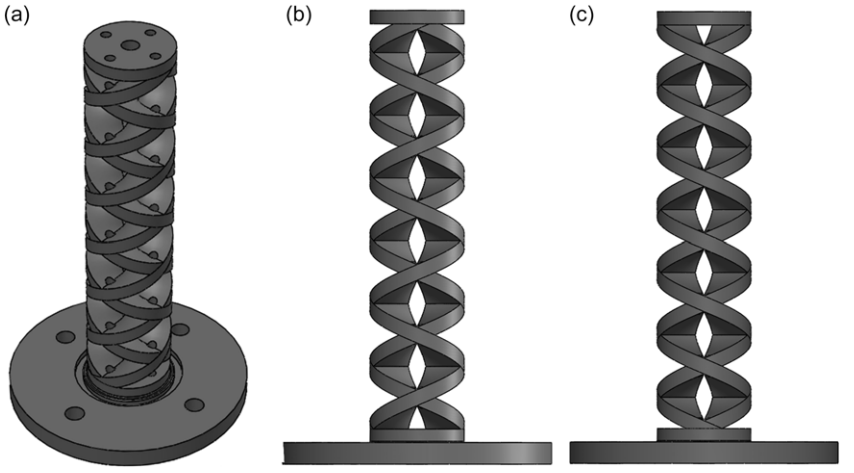


Figure 4. *CAD model of the double-helix design: (a) isometric view; (b) front view; (c) side view.*

The second design, in Fig. 2, presents a T-shaped notch pattern. Similarly to the previous design, consequent notches are rotated by 90° around the backbone axis to allow bending on two perpendicular planes. The notches include fillets on their inner sides to facilitate the printing as well as making the prototype more resistant to fatigue induced by the bending of the robot. Additionally, it allows us to obtain a more precisely comparable result during the displacement finite element analysis (FEA), avoiding stress concentration at the corners of the notches.

The third design created in this article was inspired by the design of a traditional hourglass, as illustrated in Fig. 3. It presents a circular cross-section with varying outer diameter along the backbone, whereas the inner channel diameter remains constant. The thicker sections of this design are used for tendon routing, while the thinner sections facilitate the bending of the robot. Given its axial symmetry, this design can intrinsically achieve 3D motion without requiring alternating designs like the previous two models.

The fourth design, inspired by our DNA's geometry, is based on a double helix. The two helical bodies present the same pitch and number of revolutions but differ in helix direction, as shown in Fig. 4. The resulting design, while less "discrete" in its development when compared to the V-notch and T-notch design, still results in alternating planes of bending generated by the helices' intersections alternating along the two main axes of the cross-section.

https://doi.org/10.1017/S0263574725102191 Published online by Cambridge University Press

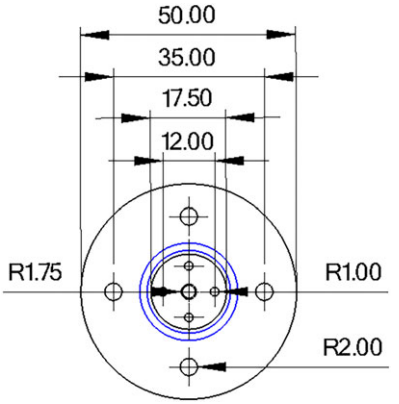


Figure 5. *Top view with characteristic dimensions for the proposed designs.*

As mentioned earlier, all four designs present the same main geometric features, with a cylindrical envelope with the same maximum outer diameter and inner channel diameter, as well as tendon-routing channel diameters and locations. These parameters are highlighted in the top view in Fig. 5, shared by all the designs (including [34]). Throughout their conception, the secondary parameters of these designs have been tuned through FEA to obtain an equivalent behavior under load. As the aim of this paper is to compare the kinematic behavior of these four designs, the objective of this analysis is only to ensure that the selected geometries do not differ (i.e., same displacement of the control point at the distal end of the backbone), rather than fully simulating motion. For the actual robot characterization, experimental data are favored over FEA here due to the challenge of modeling highly nonlinear behavior such as tendon friction and superelasticity [35]. As such, the design tuning has been set up by matching the displacement of the distal point of the backbone of each design under a set of known loads (up to 2 N) and with fixed base, through FEA, which was run in SolidWorks 2023, using the PBT material profile and with matching mesh parameters, solver, and boundary conditions (fixture on the lower surface of the base plate). As shown by the results in Fig. 6, the mechanical performance of these designs can thus be compared under equivalent conditions.

3. Actuation unit design

The selected actuation unit has been described in ref. [34] and is composed of six layers, made out of six disks with a circular shape and a diameter of 75 mm. This allows for affordable and fast manufacturing through 3D printing or laser cutting, with an estimated cost of less than €1.00 per disk and a manufacturing time of less than 10 min (3D printing) or 30 s (laser-cutting). The disks are then separated by commercial electronic board spacers, making the design adaptable in case of changes in the choice of actuators, power supply, or controller (Fig. 7). The first disk at the top of the assembly is used to fix the base of the robot as well as route the antagonistic tendons into the robot segment. Underneath, the second disk routes the tendons out of the linear motors and avoids tangling and similar routing issues. The third and fourth disks are designed to fix the four linear servomotors that actuate the system (Actuonix PQ12). These motors have a 20 mm stroke, with a maximum output of 45 N; alternative linear motors, or rotational motors with pulleys, can also be used with minimal changes to the design of the actuation unit. As a control board, a Polulu Micro Maestro 6-Channel USB Servo Controller has been selected for this work; the microcontroller is fixed to the fifth disk. Alternative solutions include Arduino or Raspberry Pi boards, potentially with a PWM driver to control up to 15 servomotors if the system's DOFs need to be scaled up. In the reported prototype, the Micro Maestro controller is linked to a computer via a USB cable to transfer the signal from the Maestro Control Center software to the motors. The fifth disk also allows the passage of wires through a 25 mm diameter hole. Finally, the six disk lodges the power supply for the controller and the linear servomotors, which comes in the shape of a 6V battery pack with

https://doi.org/10.1017/S0263574725102191 Published online by Cambridge University Press

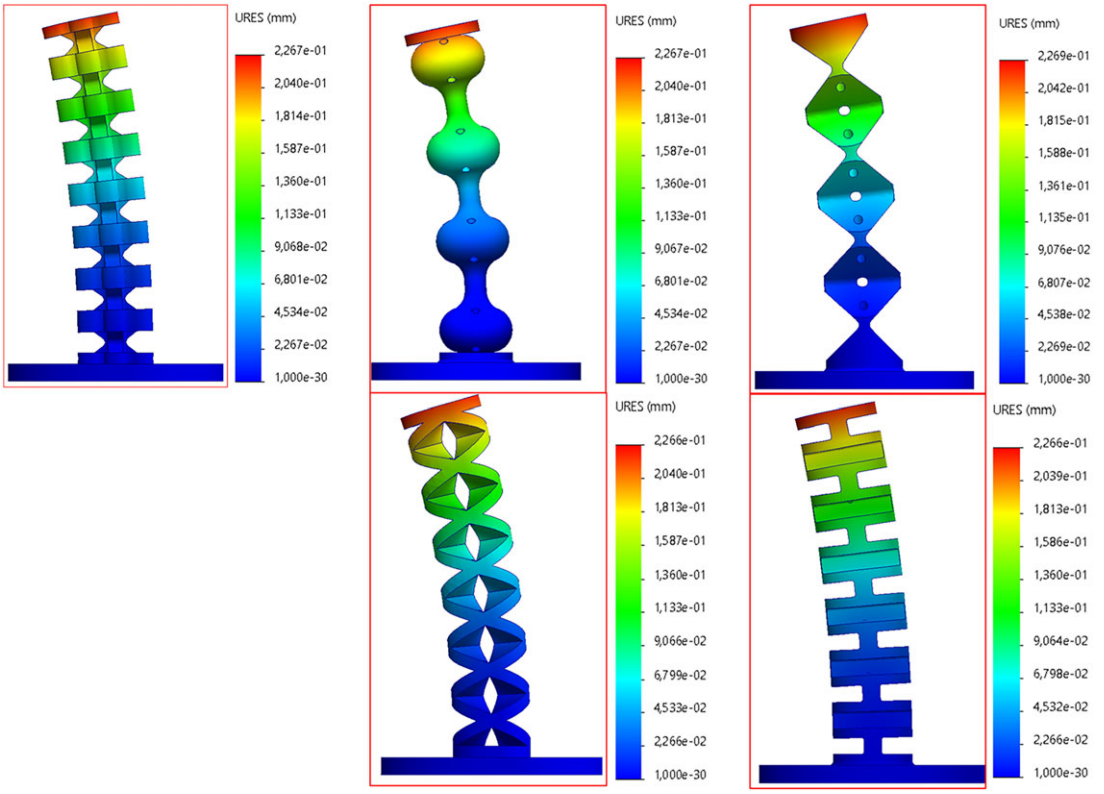


Figure 6. *Results of the finite element analysis of the four new designs as well as the design in ref. [34] (on the left), showing an equivalent displacement under load for all the systems.*

four AA batteries but can be easily replaced with a rechargeable Li-Io battery or equivalent alternatives with no impact to performance.

The cost of these designs is estimated at 265€, including the material used for the manipulators (∼15 g) with the largest expense being the motors at 58.14€ each and the Polulu Micro Maestro controller at 27.68€, which, compared to a cost of 1682 US$ (equivalent to 1504,49€) in ref. [32], denotes a significant cost reduction.

4. Operation and control

The robot has been modeled with piecewise constant curvature kinematics (PCCK), a common tool used in continuum and soft robotics [10]. Despite its limitations due to the lack of dynamic and material information on the robot, the model has been selected as the preferred tool in practical continuum robot applications because of its computational efficiency and scalability to multiple sections. PCCK describes the behavior of continuum robots by approximating the shape of their backbone to a circle arc. This assumption allows the definition of the backbone through two parameters only, namely, its angle of curvature θ and the direction of bending ϕ (see Fig. 8 for a graphical representation and Table I for the complete nomenclature). PCCK formulations can also be used to link tendon lengths, which are the actuation variables l_1, l_2, l_3, and l_4, to the motion at the robot's tip, defined by the frame $\{S\}$ with its center in (x, y, z) in the base frame$\{S_0\}$. The homogeneous transformation $\boldsymbol{T} \in \mathrm{SE}(3)$ from $\{S_0\}$ to $\{S\}$ can be expressed by

$$\mathbf{T}=\begin{bmatrix} \mathbf{R} & \mathbf{t} \\ \mathbf{0}_{1\times 3} & \mathbf{1}_{1\times 1} \end{bmatrix}, \tag{1}$$

https://doi.org/10.1017/S0263574725102191 Published online by Cambridge University Press

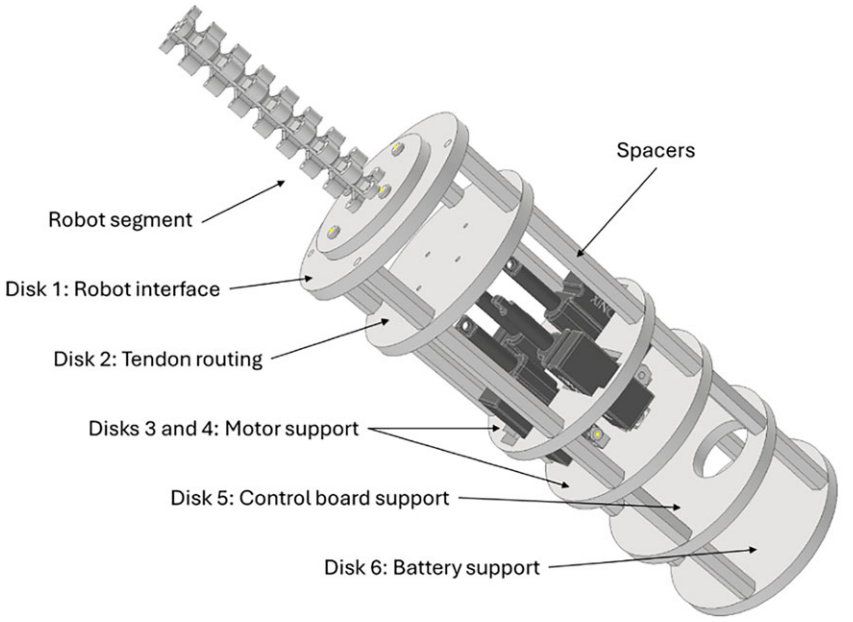


Figure 7. *CAD model of the actuation unit.*

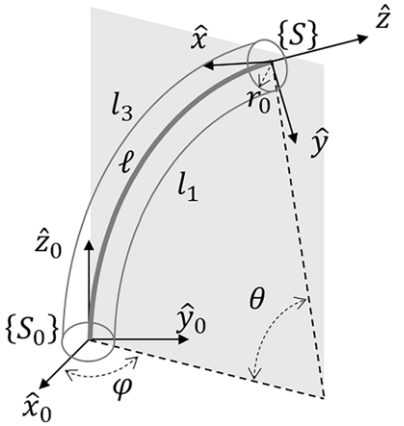


Figure 8. *Piecewise constant curvature kinematic model for a tendon-driven continuum segment.*

where $\boldsymbol{R} \in \mathrm{SO}(3)$ is the rotation and $\boldsymbol{t} \in \mathbb{R}^3$ is the translation along the segment arc. Parametrizing the motion by the bending angle θ and the direction of bending φ, as illustrated in Fig. 8, the rotation from$\{S_0\}$ to $\{S\}$ is

$$\boldsymbol{R} = \mathrm{rot}_z(\varphi) \cdot \mathrm{rot}_y(\theta) \cdot \mathrm{rot}_z(-\varphi), \tag{2}$$

and the corresponding translation is

$$\boldsymbol{t} = \frac{l}{\theta} \begin{bmatrix} \cos\varphi\,(1-\cos\theta) \\ \sin\varphi\,(1-\cos\theta) \\ \sin\theta \end{bmatrix}, \tag{3}$$

where l is the length of the backbone from {S} to {S0}. The transformation from bending angle and direction to tendon length can then be expressed as

https://doi.org/10.1017/S0263574725102191 Published online by Cambridge University Press

Table I. *Nomenclature.*

Symbol	Description
l	Segment backbone length
θ	Bending angle
φ	Direction of bending
$\{S_0\}$	Base frame
$\{S\}$	End-effector frame
$\boldsymbol{t}$	Translation vector from $\{S_0\}$ to $\{S\}$
$\boldsymbol{R}$	Rotation matrix from $\{S_0\}$ to$\{S\}$
$\boldsymbol{T}$	Transformation matrix from $\{S_0\}$ to$\{S\}$
r_0	Distance from tendon to backbone axis
l_1, l_2, l_3, l_4	Actuation tendon lengths

Table II. *Printing parameters used for TPU 95A. Please note that these parameters are the results of the authors' experience with the specific 3D printer, material, and design and might vary for different printers, filaments, and scales.*

Parameter	Value
Layer height	0.21 mm
First layer height	0.27 mm
Number of walls	2
Infill density	20%
Infill pattern	Hexagons
Printing speed	25 mm/s
Travel speed	35 mm/s
Extruding temperature	225°C
Plate temperature	55°C
Printing time (V-notches)	1h55

$$\begin{cases} l_1 = l - \theta r_0 \sin\varphi \\ l_2 = l + \theta r_0 \cos\varphi \\ l_3 = l + \theta r_0 \sin\varphi \\ l_4 = l - \theta r_0 \cos\varphi \end{cases} \tag{4}$$

This kinematic model can be used to control the motion of the prototype.

5. Results and discussion

Each prototype has been printed in standard TPU 95A with a FlashForge Adventurer 5 M printer, using the printing parameters in Table II and a 0.4 mm nozzle. In preliminary prints, manufacturing quality has been observed to go down progressively during the print, due to vibrations of the backbone induced by the load of the nozzle onto the tip of the robot (acting as a cantilever beam). To reduce these vibrations, a rigid cylindrical scaffolding structure has been inserted halfway through the printing process to reduce the exposed height of the cantilever.

A circular indentation has been added to the base of all the prototypes (highlighted in blue in Fig. 5) to nest the PLA-printed scaffolding tube, as shown in Fig. 9. This option also helps minimize the need for support material, which negatively impacts the quality of the prototype with a difficult cleaning process

https://doi.org/10.1017/S0263574725102191 Published online by Cambridge University Press



Figure 9. *Continuum robot prototyping: (a) The robot prototypes for the proposed designs (from left to right: the previous design from ref. [34] printed in white TPU, helix, hourglass, T-notches, and V-notches). (b) The PLA scaffolding structure shown during the manufacturing of the helix design.*

afterward that could damage the print itself. Further, the automatic layout of the STL in the slicer tends to place the main bending planes of the robot corresponding to the X and Y axes of the printer, further amplifying the unwanted bending behavior. Therefore, a slight rotation of the prints around the Z-axis when preparing the g-code files has also been observed to diminish the impact of the vibrations on the quality of the prototypes.

To test the designs, the robot was operated through its whole workspace, characterized by the middle and extreme points obtained by moving the servomotors in different combinations of their neutral, minimum, and maximum positions (0 mm, 10 mm, and -10 mm, respectively). The selected motion sequence contains thirteen positions, as detailed in Table III. Thanks to the kinematic model, implemented with MATLAB and used to define the trajectory in open-loop control, we have also obtained the curvature angle and the bending plane direction (θ and ϕ) for each of the thirteen configurations of the sequence, as well as the theoretical coordinates of the tip of the robots, which were then used for analysis. The behavior of the robot prototypes has instead been acquired with motion capture. To perform the acquisitions, each prototype has been attached to the actuation unit, which was then placed in an aluminum frame where cameras had been set to record the robot throughout the motion sequence in Table III, as illustrated in Figs. 10 and 11. We then used the images acquired during the experiments to extract the coordinates of the inner channel's center through MATLAB in each configuration to compare them to the theoretical results.

We tested the precision of each prototype by measuring repeatability in the center position (i.e., each motor set to 0 mm) throughout the open-loop motion sequence, obtaining five data points per cycle, with five motion cycles recorded per robot design, providing sufficient data for us to observe the efficiency of the designs. Motion was recorded both in top and side view but, given the kinematics of the system, the X and Y coordinates of the tip and sufficient to fully determine its Z coordinate as well, since it is fully coupled to the other coordinates as shown in Eq. (3). The views have been analyzed to extract the position of the distal point of the backbone through tip features, with image distortion and parallax compensated with a pixel-to-mm conversion at the base of the robot and at the tip through known geometrical features. The processed top views for an example design are presented in Fig. 12, with overall numerical results reported in Fig. 13.

For the precision results in Fig. 13(a), we obtain means between 0.51 mm for the hourglass design and 1.48 mm for the V-notches design. However, we notice a higher repeatability for the V-notches design that presents a smaller standard deviation, contrary to the T-notches design that presents wider spread

https://doi.org/10.1017/S0263574725102191 Published online by Cambridge University Press

Table III. *Motion sequence in Cartesian, configuration, and actuation space.*

l_1 (mm)	l_2 (mm)	l_3 (mm)	l_4 (mm)	θ (rad)	φ (rad)	x (mm)	y (mm)	z (mm)
0.00	0.00	0.00	0.00	0.00	0.00	0.00	0.00	80.00
−10.00	0.00	10.00	0.00	1.16	3.14	−52.59	0.00	47.78
10.00	0.00	−10.00	0.00	1.16	0.00	52.59	0.00	47.78
0.00	0.00	0.00	0.00	0.00	0.00	0.00	0.00	80.00
0.00	10.00	0.00	−10.00	1.16	1.57	0.00	52.59	47.78
0.00	−10.00	0.00	10.00	1.16	−1.57	0.00	−52.59	47.78
0.00	0.00	0.00	0.00	0.00	0.00	0.00	0.00	80.00
10.00	−10.00	−10.00	10.00	2.35	−0.78	40.98	−40.98	23.98
−10.00	10.00	10.00	−10.00	2.35	2.35	−40.98	40.98	23.98
0.00	0.00	0.00	0.00	0.00	0.00	0.00	0.00	80.00
10.00	10.00	−10.00	−10.00	2.35	0.78	40.98	40.98	23.98
−10.00	−10.00	10.00	10.00	2.35	−2.35	−40.98	−40.98	23.98
0.00	0.00	0.00	0.00	0.00	0.00	0.00	0.00	80.00

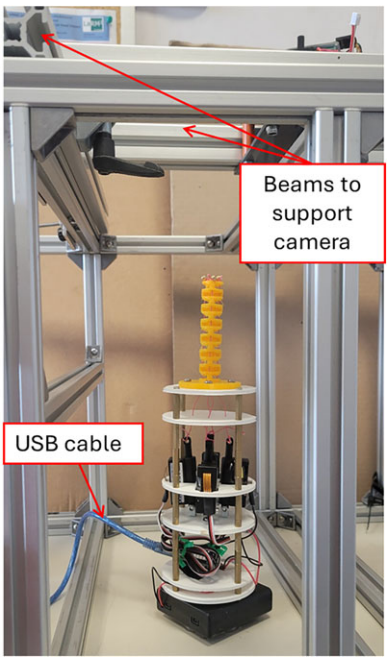


Figure 10. *Experimental setup for the top view acquisitions of the T-notch design.*

data, marking it as the design with the least repeatability. For the results in Fig. 13(b), we can observe that the experimental workspace is reduced compared to the one we expected with the PCCK model. Both results can be explained mainly by the manual attachment of the tendons to the motors, which can create a small slacking in the tendons, therefore reducing the precision and inducing a reduction of the workspace. Further causes of error include manufacturing errors during the printing process, with deformation induced by the vibrations mentioned earlier, as well as gravity-induced deformations, most notably in the T-notches design given its initial geometry. Additionally, the results could be less accurate due to image distortion and camera limitations during the acquisitions.

In the experiments, the robot prototypes show consistent behavior, as summarized in Table IV. The peak error is lower than 3.75% of the robot's length in all designs, with a median error lower than 1.9%. These values compare positively to existing literature on tendon-driven robots, which reports error rates

https://doi.org/10.1017/S0263574725102191 Published online by Cambridge University Press

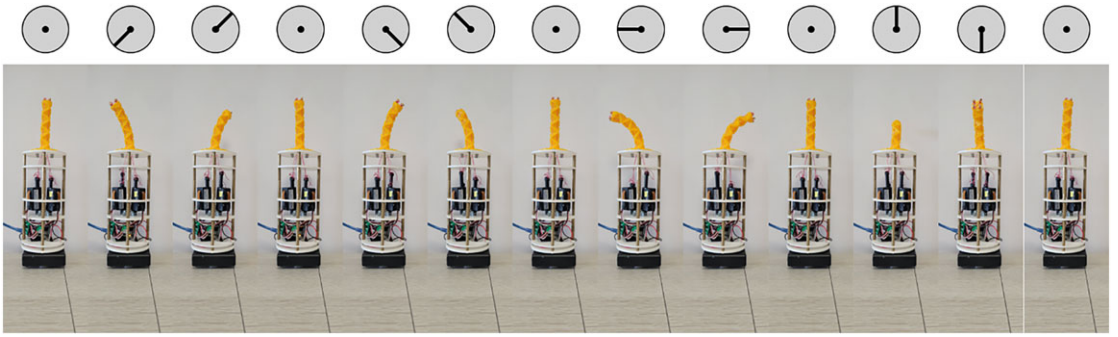


Figure 11. *Snapshots from a motion sequence of the V-notch design.*

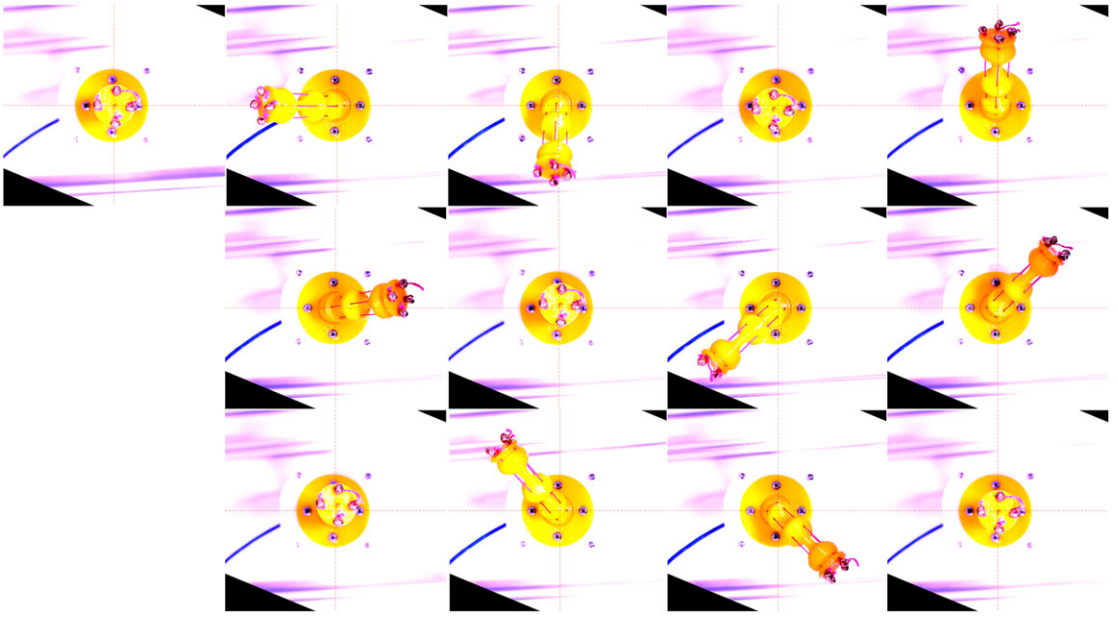


Figure 12. *Post-processed top view of the motion sequence for the hourglass design.*

up to 10% of the backbone's length [36–38]. The V-notch design shows an overall higher error, whereas T-notches present a higher variability. Both hourglass and helix performed well from the position error perspective, but the hourglass design (together with the V-notch design) shows higher misalignment (error on direction of bending), clearly noticeable in Fig. 13(b) from the right (toward positive x) bending and reflected in the values in Table IV. From the results in Fig. 13(b), the area of the projection of the workspace on the XY plane of the prototypes has been compared to the ideal value obtained through PCCK, highlighting how the T-notches design, which performs satisfactorily in all other indicators, is the worst in performance, losing up to 41% of the ideal area (mostly attributable to tendon slacking). Overall, it is difficult to identify the best of the designs: the four prototypes behaved fairly similarly with respect to the selected key performance indicators, outperforming many other designs in terms of relative positioning error but showing a more limited performance in workspace and direction alignment. Additionally, we must note that although the comparison of the bending capabilities with PCCK is an effective way to characterize the kinematic behavior and the workspace of the proposed designs, further work is needed to identify the relationship between backbone stiffness and manufacturing parameters, with a focus on infill density and pattern in addition to design variations.

https://doi.org/10.1017/S0263574725102191 Published online by Cambridge University Press

Table IV. *Design comparison.*

Design	Median error (% length)	Max position error (% length)	Mean direction error (deg)	Workspace (% to PCCK)
Helix	1.13	2.57	2.93	75.07
Hourglass	0.64	2.73	3.80	76.931
T-notches	1.04	3.70	2.96	59.03
V-notches	1.85	3.06	5.52	65.49

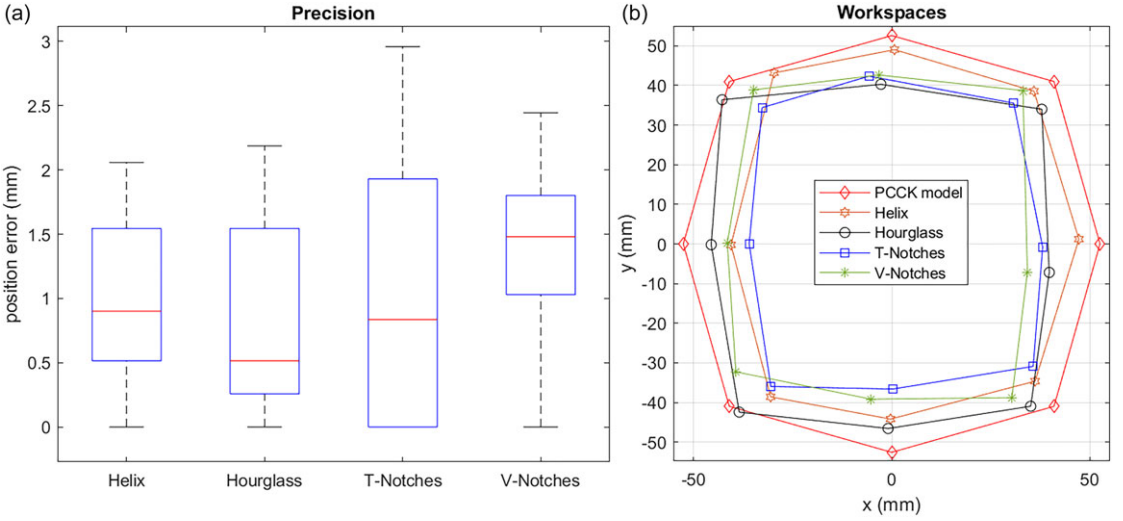


Figure 13. *Experimental results compared with the PCCK model simulation: (a) precision (median: red line; standard deviation: blue box; data range: black line); (b) workspace (top view).*

6. Conclusions

In this paper, we presented four designs of TDCR, created to reduce the manufacturing cost as well as the assembly time, making them accessible to use as educational tools for continuum robotics, as well as encourage the development and uptake of this technology. The main contributions of the paper can be summarized as:

- The four proposed monolithic designs, which can be printed in a single part with TPU or other flexible material, highly reduce the cost and manufacturing/assembly time when compared to previous TDCR designs with segmented backbone and vertebrae while maintaining similar performance.
- A modular, easy-to-assemble actuation unit to actuate TDCR. This actuation unit design can also be printed or laser cut, making the manufacturing cost affordable, and relies on modular commercial components that allow for easy adaptation to different actuators, controllers, power supplies, and robot designs.
- The experimental characterization of the robot prototypes. Each design was tested through a sequence of 13 positions at the borders and in the center of the workspace; each sequence was repeated five times per prototype. The results highlight a peak error lower than 3.75% of the backbone's length for all designs, with a median error lower than 1.9% (compared to errors up to 10% in literature with the open-loop control of a single segment).

https://doi.org/10.1017/S0263574725102191 Published online by Cambridge University Press

However, we still note a decrease in expected workspace for the V-notches and T-notches due mainly to tendon slacking, as well as print quality in the case of the T-notches design. Future developments will be oriented toward improving tendon tension, which has been observed to be the key source of error. Even though tension control could be implemented, having hardware tensioners could solve tendon slacking in a much more reliable and effective way, also restoring part of the workspace loss observed with respect to the ideal PCCK model.

Supplementary material. The supplementary material for this article can be found at https://doi.org/10.1017/S0263574725102191.

Author contributions. CGK, NP, and MR conceived and designed the study. CK and NP designed and manufactured the prototypes and conducted data gathering. CK performed statistical analyses. CK and MR wrote the article.

Financial support. This research received no specific grant from any funding agency, commercial, or not-for-profit sectors.

Competing interests. The authors declare no conflicts of interest exist.

Ethical approval. Not applicable.

References

[1] P. E. Dupont, N. Simaan, H. Choset and H. Rucker, "Continuum robots for medical interventions," *Proc. IEEE* **110**(7), 847–870 (2022). doi: 10.1109/jproc.2022.3141338.
[2] J. Burgner-Kahrs, D. C. Rucker and H. Choset, "Continuum robots for medical applications: A survey," *IEEE Trans. Rob.* **31**(6), 1261–1280 (2015). doi: 10.1109/tro.2015.2489500.
[3] Y. Yamauchi, Y. Ambe, H. Nagano, M. Konyo, Y. Bando, E. Ito, S. Arnold, K. Yamazaki, K. Itoyama, T. Okatani, H. G. Okuno and S. Tadokoro, "Development of a continuum robot enhanced with distributed sensors for search and rescue," *ROBOMECH J.* **9**(1) (2022). doi: 10.1186/s40648-022-00223-x.
[4] P. A. Der Maur, B. Djambazi, Y. Haberthür, P. Hörmann, A. Kübler, M. Lustenberger, S. Sigrist, O. Vigen, J. Förster, F. Achermann, E. Hampp, R. K. Katzschmann and R. Siegwart , Roboa: Construction and Evaluation of a Steerable Vine Robot for Search and Rescue Applications. [online] IEEE Xplore (2021). doi:10.1109/robosoft51838.2021.9479192.
[5] A. Mohammad, M. Russo, Y. Fang, X. Dong, D.ş Axinte and J. Kell, "An efficient follow-the-leader strategy for continuum robot navigation and coiling," *IEEE Rob. Autom. Lett.* **6**(4), 7493–7500 (2021). doi: 10.1109/lra.2021.3097265.
[6] X. Dong, M. Wang, A. Mohammad, W. Ba, M. Russo, A. Norton, J. Kell and D. Axinte, "Continuum robots collaborate for safe manipulation of high-temperature flame to enable repairs in challenging environments," *IEEE/ASME Trans. Mechatron.* **27**(5), 4217–4220 (2022). doi: 10.1109/TMECH.2021.3138222.
[7] A. Yeshmukhametov, K. Koganezawa, Y. Yamamoto, Z. Buribayev, Z. Mukhtar and Y. Amirgaliyev, "Development of continuum robot arm and gripper for harvesting cherry tomatoes," *Appl. Sci.* **12**(14), 6922 (2022). doi: 10.3390/app12146922.
[8] J. Shintake, V. Cacucciolo, D. Floreano and H. Shea, "Soft robotic grippers," *Adv. Mater.* **30**(29), 1707035 (2018). doi: 10.1002/adma.201707035.
[9] B. S. Homberg, R. K. Katzschmann, M. R. Dogar and D. Rus, Haptic identification of objects using a modular soft robotic gripper. [online] IEEE Xplore (2015). doi:10.1109/IROS.2015.7353596.
[10] M. Russo, S. M. H. Sadati, X. Dong, A. Mohammad, I. D. Walker, C. Bergeles, K. Xu and D. A. Axinte, "Continuum robots: An overview," *Adv. Intell. Syst.* **5**(5), 2200367 (2023). doi: 10.1002/aisy.202200367.
[11] Z. Mitros, S. M. H. Sadati, R. Henry, L. Da Cruz and C. Bergeles, "From theoretical work to clinical translation: Progress in concentric tube robots," *Ann. Rev. Control Rob. Auton. Syst.* **5**(1) (2021). doi: 10.1146/annurev-control-042920-014147.
[12] H. Alfalahi, F. Renda and C. Stefanini, "Concentric tube robots for minimally invasive surgery: Current applications and future opportunities," *IEEE Trans. Med. Rob. Bionics* **2**(3), 410–424 (2020). doi: 10.1109/tmrb.2020.3000899.
[13] M. Li, R. Kang, S. Geng and E. Guglielmino, "Design and control of a tendon-driven continuum robot," *Trans. Inst. Meas. Control* **40**(11), 3263–3272 (2018). doi: 10.1177/0142331216685607.
[14] V. Pachouri and P. M. Pathak, "Design and modeling of a planar-to-spatial tendon-driven continuum manipulator subjected to uncertain forces," *Rob. Auton. Syst.* **170**, 104551–104551 (2023). doi: 10.1016/j.robot.2023.104551.
[15] J. Greer, T. Morimoto, A. Okamura and E. Hawkes, "Series Pneumatic Artificial Muscles (spams) and Application to a Soft Continuum Robot," *2017 IEEE International Conference on Robotics and Automation (ICRA)* (2017).
[16] M. E. Giannaccini, C. Xiang, A. Atyabi, T. Theodoridis, S. Nefti-Meziani and S. Davis, "Novel design of a soft lightweight pneumatic continuum robot arm with decoupled variable stiffness and positioning," *Soft Rob.* **5**(1), 54–70 (2018). doi: 10.1089/soro.2016.0066.
[17] K.-Y. Kim, H.-S. Woo and J. Suh, Design and Evaluation of a Continuum Robot with Discreted link joints for Cardiovascular Interventions (2018). doi: 10.1109/biorob.2018.8487633

https://doi.org/10.1017/S0263574725102191 Published online by Cambridge University Press

[18] Q. Guan, F. Stella, C. D. Santina, J. Leng and J. Hughes J, "Trimmed helicoids: An architectured soft structure yielding soft robots with high precision, large workspace, and compliant interactions," *Npj Rob.* **1**(1) (2023). doi: 10.1038/s44182-023-00004-7.
[19] L. H. Blumenschein, M. M. Coad, D. A. Haggerty, A. M. Okamura and E. W. Hawkes, "Design, modeling, control, and application of everting vine robots," *Front. Rob. AI* **7** (2020). doi: 10.3389/frobt.2020.548266.
[20] A. Ataka, T. Abrar, F. Putzu, H. Godaba and K. Althoefer, "Model-based pose control of inflatable eversion robot with variable stiffness," *IEEE Rob. Autom. Lett. [online]* **5**(2), 3398–3405 (2020). doi: 10.1109/LRA.2020.2976326.
[21] Z. Song, Z. Wang, B. Liu, Y. Song and X. Zhang, "A soft gripper based on pneunets structure with stiffness-variable-enhanced load capacity for object grasping," *Sens. Actuators A Phys.*, 116253–116253 (2025). doi: 10.1016/j.sna.2025.116253.
[22] J. Yoon and D. Yun, "Geometrical parameters investigation of a zig-zag soft pneumatic actuators," *Adv. Eng. Mater.* **26**(20) (2024). doi: 10.1002/adem.202400560.
[23] D. A. Troncoso, J. A. Robles-Linares, M. Russo, M. A. Elbanna, S. Wild, X. Dong, A. Mohammad, J. Kell, A. D. Norton and D. Axinte, "A continuum robot for remote applications: From industrial to medical surgery with slender continuum robots," *IEEE Rob. Autom. Mag.* **30**(3), 94–105 (2023). doi: 10.1109/MRA.2022.3223220.
[24] R. M. Grassmann, S. Lilge, P. Le and J. Burgner-Kahrs, "Ctcr Prototype Development: An Obstacle in the Research Community?," *Robotics Retrospectives Workshop at RSS* (2020).
[25] B. Zhu, X. Zhang, H. Zhang, J. Liang, H. Zang, H. Li and R. Wang, "Design of compliant mechanisms using continuum topology optimization: A review," *Mech. Mach. Theory* **143**, 103622 (2020). doi: 10.1016/j.mechmachtheory.2019.103622.
[26] T. A. Khalil, S. Habib, S. G. Seadby and S. A. Maged, "A structural optimization analysis of cable-driven soft manipulator," *Int. J. Adv. Rob. Syst.* **21**(2) (2024). doi: 10.1177/17298806241246886.
[27] A. B. Clark, V. Mathivannan and N. Rojas, "A continuum manipulator for open-source surgical robotics research and shared development," *IEEE Trans. Med. Rob. Bionics* **3**(1), 277–280 (2021). doi: 10.1109/tmrb.2020.3041391.
[28] J. L. Sitler and L. Wang, "A modular open-source continuum manipulator for underwater remotely operated vehicles," *J. Mech. Rob.* **14**(6) (2022). doi: 10.1115/1.4054309.
[29] A. Beaudette, L. Gerez, D. Holland, S. Berdnt and E. J. Park, Soft Robotics Toolkit. [online] softroboticstoolkit.com. Available at https://softroboticstoolkit.com/home
[30] D. P. Holland, E. J. Park, P. Polygerinos, G. J. Bennett and C. J. Walsh, "The soft robotics toolkit: Shared resources for research and design," *Soft Rob.* **1**(3), 224–230 (2014). doi: 10.1089/soro.2014.0010.
[31] Open Continuum Robotics website [online] Available at: https://www.opencontinuumrobotics.com
[32] R. M. Grassmann, C. Shentu, T. Hamoda, P. T. Dewi and J. Burgner-Kahrs, "Open continuum robotics–one actuation module to create them all," *Front. Rob. AI* **11** (2024). doi: 10.3389/frobt.2024.1272403.
[33] M. A. Graule, C. B. Teeple, T. P. mccarthy, G. R. Kim, R. C. St. Louis and R. J. Wood , Somo: Fast and Accurate Simulations of Continuum Robots in Complex Environments. [online] IEEE Xplore (2021). doi: 10.1109/IROS51168.2021.9636059.
[34] N. Perugini and M. Russo, "A monolithic tendon-driven continuum robot design for easy 3D printing and assembly," *Mech. Mach. Sci.*, 215–223 (2024). doi: 10.1007/978-3-031-64553-2_25.
[35] L. Raimondi, M. Russo, X. Dong and D. Axinte, "Understanding friction and superelasticity in tendon-driven continuum robots," *Mechatronics* **104**, 103241 (2024). doi: 10.1016/j.mechatronics.2024.103241.
[36] C. Bishop, M. Russo, X. Dong and D. Axinte, "A novel underactuated continuum robot with shape memory alloy clutches," *IEEE Trans. Mechatron.* **27**(6), 5339–5350 (2022). doi: 10.1109/TMECH.2022.3179812.
[37] J. Barrientos-Diez, M. Russo, X. Dong, D. Axinte and J. Kell, "Asymmetric continuum robots," *IEEE Rob. Autom. Lett.* **8**(3), 1279–1286 (2023). doi: 10.1109/LRA.2023.3238890.
[38] Y. Fang, X. Dong, A. Mohammad and D. Axinte, "Design and control of a multiple-section continuum robot with a hybrid sensing system," *IEEE/ASME Trans. Mechatron.* **28**(3), 1522–1533 (2023). doi: 10.1109/tmech.2022.3229.

Cite this article: C.G. Kierbel, N. Perugini and M. Russo (2025). "A comparison of monolithic 3D-printed tendon-driven continuum robot designs", Robotica **43**, 3888–3901. https://doi.org/10.1017/S0263574725102191

https://doi.org/10.1017/S0263574725102191 Published online by Cambridge University Press